

Solving the max-3-cut problem using synchronized dissipative networks

S. L. Harrison,^{1,*} H. Sigurdsson,^{1,2} and P. G. Lagoudakis^{2,1,†}

¹*School of Physics and Astronomy, University of Southampton, Southampton, SO17 1BJ, United Kingdom*

²*Skolkovo Institute of Science and Technology, Moscow, Bolshoy Boulevard 30, bld. 1, 121205, Russia*

(Dated: July 14, 2020)

Many computational problems are intractable through classical computing and, as Moore's law is drawing to a halt, demand for finding alternative methods in tackling these problems is growing. Here, we propose a hardware implementable optical optimization heuristic for the NP-Hard max-3-cut problem based on a synchronized network of exciton-polariton condensates. The condensate network dynamical transients provide optically-fast annealing of the XY Hamiltonian to which we apply Goemans and Williamson random hyperplane technique, discretizing the XY ground state spin configuration to serve as ternary decision variables for an approximate optimal solution to the max-3-cut problem. Applications of our optical system are investigated in image segmentation tasks and constrained via minimization in circuit design, both showing good performance. Our work takes a step towards overcoming the limitation faced by Ising machines whose binary decision variables can only be mapped to the max-2-cut problem, whereas we realise an optical based XY machine to provide an approximate solution to the max-3-cut problem.

I. INTRODUCTION

Complexity in nature is as widespread as it is diverse, and with the turn of the age there has been a rapid rise in strategies designed to tackle complex problems deemed too cumbersome for conventional Turing-based computers to solve. Although highly efficient in parallel form, computers in the Von-Neumann architecture must iteratively store and access memory to complete their computational tasks. This limiting feature is known as the *Von-Neumann Bottleneck*. In 1965, Gordon E. Moore (co-founder of Intel), correctly predicted that the number of transistors on a circuit board would double biannually, as computer price would half [1]. Like any exponential growth, this growth was unsustainable and after five decades, it began to flatten and the ability to pack additional transistors onto a chip now draws to a halt [2] due to transistor size pushing the limits of lithographic techniques, heating problems, and approaching quantum effects. Scientific fields devoted to climate change [3–5], drug design [6], development of new materials and batteries [7], and so on, are reliant on the increase of computational power for solving complex problems.

A computational problem is said to be intractable when no efficient algorithm exists to solve it. A class of such problems is the NP-complete class, where an estimated solution can be verified in polynomial time, though no algorithm exists to calculate an exact solution. As these problems are so widely encountered [8], they are often approached using approximation algorithms or heuristic methods such as semi-definite programming [9–11], genetic algorithms [12], and nature inspired heuristic algorithms [13, 14]. However, instead of building approximate algorithms to get a near-optimum solution to

the problem one can instead pit nature herself against it. When dealing with optimization problems which are concerned with minimizing a cost function, an alternative to classical computation is mapping the optimization problem to a physical system that relaxes to the ground state of its energy landscape corresponding to the global minimum of the cost function. Optical based systems, which are being regarded as the next possible generation of both quantum [15] and classical computational devices [16], have generated much interest with photonic-based classical annealers already realized for both Ising [17–23] and XY spin Hamiltonians [24–28], waveguide networks for the subset sum problem [29], and digital degenerate cavity laser for the phase retrieval problem [30]. Even when simulated on a standard computer, the update equations themselves describing the dynamics of such nonlinear oscillatory networks possess amazing capabilities in finding near-optimum solutions to hard problems [31, 32].

In this work, we investigate a type of optical computational device based on planar networks of exciton-polariton condensates in semiconductor microcavities and their potential to optimise a maximum cut computational problem with focus on two types of real world applications. Utilizing the recent developments connecting the dissipative nature of polariton condensate dynamics to minimization of the XY model [25, 31, 33] we apply a random hyperplane method to bin the XY ground state spins obtained from our polariton network into ternary decision variables [10, 34]. We proceed to map the NP-Hard max-3-cut (M3C) optimisation problem [35] to the energy minimization of a ternary phase-discretized XY model, which is then near-optimally solved using the decision variables obtained from the standard XY model. Unlike Ising machines, which can only be mapped to the max-2-cut problem [19, 36], the continuous degree of freedom of the variables (spins) in XY systems makes their approximate partition into higher dimensional decision variables possible, with a direct a mapping to the M3C problem. Variants on the max-cut problem have many

* S.L.Harrison@soton.ac.uk

† Pavlos.Lagoudakis@soton.ac.uk

applications, including social network modelling [37], statistical physics [36, 38], portfolio risk analysis [39], circuit design [38, 40], image segmentation [41] (including medical image analysis [42]), network design [43], map coloring [44, 45] and facility layout design [46]. We demonstrate this heuristic in the applications of image segmentation and constrained via minimization in circuit design with networks of synchronized microcavity polariton condensates [33], which we simulate using the generalized Gross-Pitaevskii equation (GPE).

II. RESULTS

Mapping the M3C Problem to a Phase-Discretized XY Model

The M3C problem is as follows: given an undirected graph $\mathcal{G} = (\mathcal{V}, \mathcal{E})$, the M3C is the partition of vertices \mathcal{V} into three subsets, such that the sum of all edge weights \mathcal{E} that connect between different subsets is maximized. We denote the number of vertices with $|\mathcal{V}|$. Following similar arguments presented by Barahona for an Ising spin system [38] we will show a map from minimizing the energy of a ternary XY spin system to the maximization of a M3C problem. The ternary spin system is written as follows,

$$\mathbf{s} = \begin{pmatrix} \cos(\theta) \\ \sin(\theta) \end{pmatrix}, \quad \theta \in \left\{0, \frac{2\pi}{3}, \frac{4\pi}{3}\right\}. \quad (1)$$

Here, $\mathbf{s} \in \mathbb{R}^2$ is a vector that can pick up three distinct orientations. We call these vectors *spins* in analogy with Ising spin systems which are binary in comparison (i.e., $\theta \in \{0, \pi\}$). For a set of spins and a set of couplings $J_{ij} = J_{ji} \in \mathbb{R}$ we define a Hamiltonian,

$$H = - \sum_{ij} J_{ij} \mathbf{s}_i \cdot \mathbf{s}_j. \quad (2)$$

Here, $\mathbf{s}_i \cdot \mathbf{s}_j$ is the dot product between the spins. It is easy to see that in our ternary system for any two spins we have $\mathbf{s}_i \cdot \mathbf{s}_j = \cos(\theta_i - \theta_j) \in \{1, -\frac{1}{2}\}$. This model is also known as the $q = 3$ vector Potts model which has been studied in statistical mechanics and quite recently in the context of exciton-polariton condensates [47]. When $\theta_i \in [-\pi, \pi)$ then Eq. (2) is just the standard XY model,

$$H_{XY} = - \sum_{ij} J_{ij} \cos(\theta_i - \theta_j), \quad \theta_i \in [-\pi, \pi). \quad (3)$$

Let us now define an undirected graph $\mathcal{G} = (\mathcal{V}, \mathcal{E})$ with edges \mathcal{E} connecting vertices \mathcal{V} , where \mathcal{V} contain the ternary spins \mathbf{s} from Eq. (1). Each edge connecting vertex \mathcal{V}_i and \mathcal{V}_j , with corresponding spins s_i and s_j , is assigned a weight J_{ij} . We define three sets of spins corresponding to the three orientations of θ_i ,

$$\mathcal{V}_n = \left\{ i \in \mathcal{V} \mid s_i = \frac{2\pi n}{3} \right\}, \quad n = 0, 1, 2. \quad (4)$$

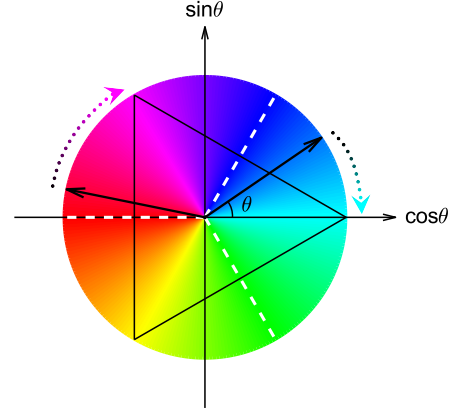


Figure 1. Random hyperplane method for binning the XY ground state phases to the nearest ternary counterpart. Here we have chosen the hyperplane (white dashed lines) as represented by the vertices of the black unit triangle within the colored unit disc in the complex plane, with example phasors (black arrows) at $\theta = 0.6$ and $\theta = 2.9$ radians rounded to 0 and $\frac{2\pi}{3}$ respectively, as depicted by the dotted gradient-color arrows. The boundaries for discretizing phases into each spin subset are shown by white dashed lines at $\theta = \frac{\pi}{3}, \pi$ and $\frac{5\pi}{3}$.

Let us define \mathcal{E}_n as the set of edges connecting spins within each set \mathcal{V}_n and $\delta\mathcal{E}$ as the set of edges connecting spins between different sets of vertices. We can then rewrite Eq. (2) in the following manner,

$$H = - \sum_{i,j \in \mathcal{E}_n} J_{ij} + \frac{1}{2} \sum_{i,j \in \delta\mathcal{E}} J_{ij}. \quad (5)$$

By defining the sum total of all the edges $C = \sum_{i,j \in \mathcal{E}} J_{ij}$, we then have,

$$H + C = \frac{3}{2} \sum_{i,j \in \delta\mathcal{E}} J_{ij}. \quad (6)$$

Since C is invariant on the spin configuration, it can be seen that minimizing Eq. (2) is the same as maximizing a M3C problem by redefining $J_{ij} = -\mathcal{W}_{ij}$, where \mathcal{W}_{ij} is the weight of the edge connecting \mathcal{V}_i and \mathcal{V}_j ,

$$\min \left[- \sum_{ij} J_{ij} \mathbf{s}_i \cdot \mathbf{s}_j \right] \leftrightarrow \max \left[\sum_{i,j \in \delta\mathcal{E}} \mathcal{W}_{ij} \right]. \quad (7)$$

As pointed out by Frieze and Jerrum [48] such a mapping is possible between a max- k -cut problem and a system of spins in the vertices of an equilateral simplex in \mathbb{R}^{k-1} . For the max-2-cut problem the corresponding simplex is a line with vertices $\theta = \{0, \pi\}$ which is the reason an Ising system maps directly to the max-2-cut [36]. For the M3C problem the simplex is an equilateral triangle inscribed by the unit circle like shown in Fig. 1. The ground state of the standard XY Hamiltonian [Eq. (3)], which can be approximately solved using the polariton network [25], is then discretized into the ternary XY system [Eq. (2)] by binning the continuous XY spins into

their closest ternary counterparts corresponding to the vertices of the inscribed triangle. Such a random hyperplane method is a semi-definite relaxation program which was first studied in computer science by Goemans and Williamson for the max-2-cut problem [10] and later for the M3C [34]. It should be noted that it is not a hyperplane (white dashed lines in Fig. 1) which bins the XY spins here but rather a generalization of one used in [10]. For purity we will refer to the white dashed lines as our “hyperplane” and its random realizations as different rotations of the white dashed lines (or equivalently the black triangle) in the unit disc. We point out that the minimization of the ternary [Eq. (2)] and continuous [Eq. (3)] XY system share the same relaxation procedure to a semi-definite program [10, 11] underlining the common point of finding the ground states of the two systems.

The mapping is shown visually in Fig. 2 using the XY ground state of the anti-ferromagnetic (AFM) house pattern, as previously studied in [28] using degenerate laser cavities. Here, AFM refers to anti-phase synchronization $\theta_i - \theta_j = \pi$ between two condensates and corresponds to $J_{ij} < 0$ in Eqs. (2) and (3). The contrary, ferromagnetic (FM) alignment refers to the in-phase condensate synchronization $\theta_i - \theta_j = 0$, corresponding to $J_{ij} > 0$ interactions. The AFM house graph shown in Fig. 2(a) consists of vertices (colored discs) arranged in the illustrated fashion with equally weighted AFM edges $J_{ij} = J < 0$. Here, we calculate the XY ground state using the classical basin hopping optimization method [49] with the ground state angles θ_i given by the numbers inside the discs. Applying our random hyperplane method the angles are binned into the three vertices of Eq. (1) and shown in Fig. 2(b). We then apply our ternary XY outcome to the M3C through Eq. (7) which dictates that the partitions (and their cuts) follow the colored regions shown in Fig. 2(b). To illustrate that the maximum weight has been obtained through the ground state of the XY system, we plot in Fig. 2(d) the found weight (red line) against the distribution of possible weights (blue bars) in the M3C of the house graph (obtained from 1000 random samples of θ_i) which indeed confirms that the maximum weight has been found.

To investigate whether a network of polariton condensates, belonging to a macroscopic wavefunction $\Psi(\mathbf{r})$, will give the same outcome as the basin hopping method we show the resultant steady state phase map $\theta(\mathbf{r}) = \arg(\Psi(\mathbf{r}))$ in Fig. 2(e,g) from a simulation of the 2DGPE using stochastic initial conditions (see Eq. (A1) in the Appendix) where $\mathbf{r} = (x, y)$ represents the 2D spatial coordinate of the semiconductor microcavity system. We point out that the words ‘phase’ and ‘angle’ carry the same meaning here since phase is defined by its angle on the complex plane unit circle. The simulation takes into account the presence of nonresonant lasers [see Fig. 2(e)] which generate co-localized high condensate densities $|\Psi(\mathbf{r})|^2$ [see Fig. 2(f)] which adopt a phase configuration $\theta(\mathbf{r})$ [see Fig. 2(g)] minimizing the XY Hamil-

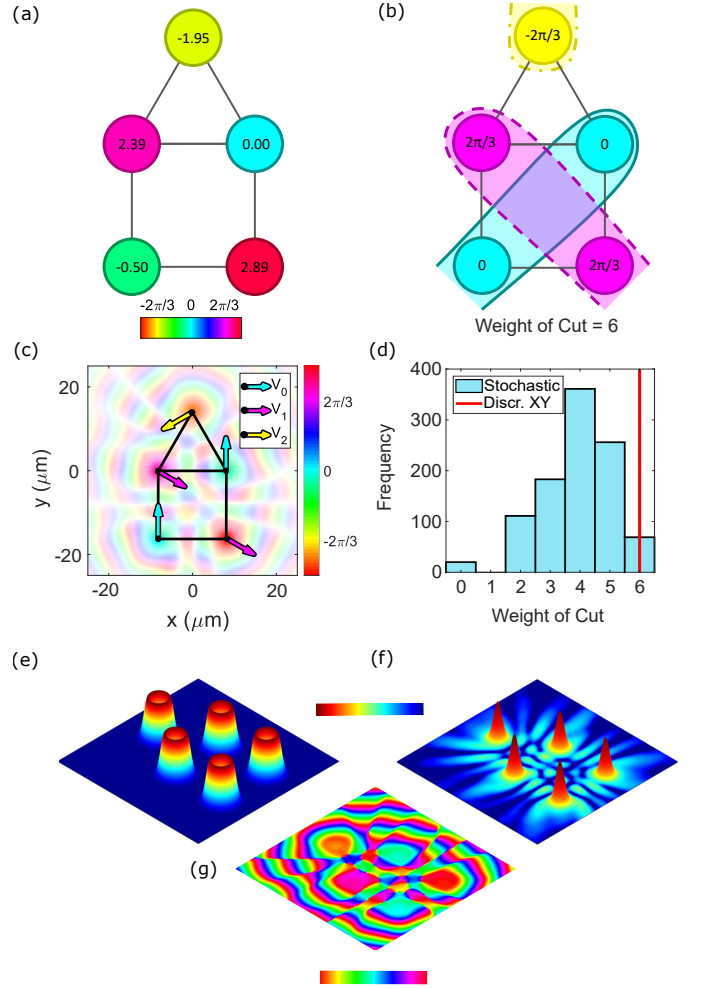


Figure 2. Optimization of the M3C problem for the AFM house graph obtained through maximizing the XY ground state first and then projecting said spins into their ternary values. (a) The XY ground state of the AFM house configuration where the numbers represent the angles θ_i of the vertices calculated using the classical basin hopping method with coupling strengths $J_{ij} = -1$; (b) the ternary mapping of the phases in (a), giving the maximum M3C weight. (c) 2D phase map from GPE simulation of optically trapped polariton condensates [33] in the same AFM house configuration as (a) with arrows to showing the discretized XY phase into subsets $\mathcal{V}_{0,1,2}$ and transparency proportional to the polariton density; (d) histogram of the M3C weights from the corresponding house graph using 1000 random samples of partitioning; (e) optical pump profile $P(\mathbf{r})$; (f) condensate density $|\Psi(\mathbf{r})|^2$ (logarithmic color scale), and (g) condensate phase map $\theta(\mathbf{r})$ as used in the simulation of the house configuration in (c). The cyan, magenta and yellow arrows represent the subsets $\mathcal{V}_{0,1,2}$ respectively.

tonian [25]. The couplings J_{ij} defining Eqs. (2) and (3) are determined from the interference between adjacent condensate maxima in Fig. 2(f) which corresponds to the spatial coordinates \mathbf{r}_i programmed into optical laser network shown in Fig. 2(e) [see Eq. (A4) in the Appendix]. The details of choosing the right spatial coordinates for

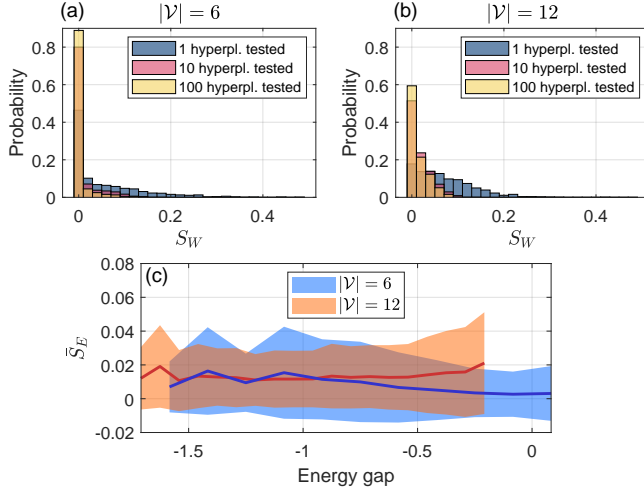


Figure 3. Performance check on the polariton network against the M3C problem in a densely connected graph with (a) $|\mathcal{V}| = 6$ vertices and (b) $|\mathcal{V}| = 12$ vertices showing an expected drop in performance as the graph increases yet still maintaining peak success at $S = 0$. The expected (mean) performances are $\bar{S}_W = 0.53\%$ and 1.38% for (a) and (b) respectively. With more random hyperplanes tested (different rotations of the triangle in Fig. 1) to bin the XY spins into their ternary counterparts the probability of finding the right solution increases. (c) Mean performance error \bar{S}_E (whole lines) plotted against the ground state energy gap $\min(H) - \min(H_{XY})$ indicating weak dependence when the energies are different. Shaded area denotes the standard deviation. Horizontal axis is given in units of $|\mathcal{V}|\sigma$ where σ is the standard deviation of J_{ij} (W_{ij}).

the lasers to represent the weights J_{ij} in Eqs. (2) and (3) was previously discussed in Ref. [33]. The five laser pump spots and the corresponding five maxima in the condensate density $|\Psi(\mathbf{r})|^2$ represent the vertices in our house graph and the phases $\theta(\mathbf{r}_i) = \theta_i$ used to obtain the approximate ground state to Eq. (3). We observe that our results in Figs. 2(c,g) converge into a phase pattern very close to the angle configuration in Fig. 2(a) and exactly into a ternary configuration like in Fig. 2(b). The transparency in Fig. 2(c) is proportional to the particle density $|\Psi(\mathbf{r})|^2$ in order to demonstrate the interference between interacting condensates and to show that the majority of particles are located at their respective pump spot locations \mathbf{r}_i [see Fig. 2(e)].

The results shown in Fig. 2 underline the promise of applying exciton-polariton systems to solve the M3C problem. But in order to verify the quality of the method we must look into its statistics by testing against many different configurations \mathcal{W}_{ij} of weighted edges in the graph and different initial conditions for the polariton condensates. In Fig. 3 we compare the near-optimum solution to the M3C coming from the polariton network, obtained by solved a discretized version of the 2DGPE which we label 0DGPE [see Eq. (A5) in the Appendix] for computational efficiency, against the correct solution found using a brute force method. We de-

fine a normalized distance from the optimum solution as $S_W = (W_{BF}^{\max} - W_{GP}) / (W_{BF}^{\max} - W_{BF}^{\min})$ where $W_{BF}^{\max(\min)}$ is the maximum (minimum) weight belonging to a 3-cut in the graph \mathcal{G} found through the brute force method and W_{GP} is the value found by the polariton network. With this metric $S_W = 0$ means that the system has found the correct maximum cut whereas $S_W = 1$ means it found the smallest cut. We use 1000 dense random configurations \mathcal{W}_{ij} (normally distributed with zero mean) and numerically solve the 0DGPE from stochastic initial conditions for each configuration to obtain the phases θ_i . Increasing the number of random hyperplane tested results in increased performance which can be intuitively understood from the fact that while Eq. (3) is independent of global rotation of the spins $\theta_i \rightarrow \theta_i + \phi$ the procedure of binning the XY spins to evaluate Eq. (2) is not. Therefore several different hyperplane orientations should be attempted in order to obtain the best value to the M3C. We point out that, to our knowledge, there is no analytical estimate on the “performance guarantee” of the simulated polariton network in finding the XY ground state and therefore the performance guarantee of finding the M3C cannot be ascertained except through numerical methods.

We additionally investigate whether the performance of the system depends on the energy gap between the ground states of H [Eq. (2)] and H_{XY} [Eq. (3)] in Fig. 3(c). We use the polariton network to find the approximate ground state energy of H_{XY} whereas we find the ground state energy of H using a brute force method. Again, the normalized mean energy distance is defined $S_E = (H_{BF}^{\max} - H_{GP}) / (H_{BF}^{\max} - H_{BF}^{\min})$ where $H_{BF}^{\max(\min)}$ are maximum and minimum energy from Eq. (2) and H_{GP} is the estimated ground state energy of H using the random hyperplane method on the polariton network. The results in Fig. 3(c) show the mean \bar{S}_E distance from the optimal solution at different energy gaps along with its standard deviation (evaluated over 1000 random W_{ij}). The results imply good performance with no significant dependence on the energy gap between the two Hamiltonians.

Image Segmentation

The M3C problem can be used to segment an image into 3 objects or regions [50]. When formulating a graph from an image, the vertices and edges represent pixels and their relative similarity respectively. When selecting vertices, all pixels or a smaller sample can be included, with connectivity to neighbors within a given radius. To define the edge weights, a weighted average is taken over properties such as color, brightness, texture, spatial proximity and number of sharp edges between pixels, in addition to setting a threshold weight [42, 50–52]. In this work, we consider color, brightness and spatial proximity using a variety of procedures to enumerate the edge weights for the M3C problem.

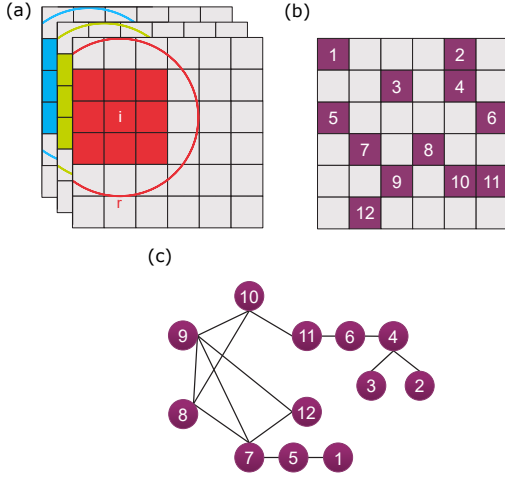


Figure 4. Visual representations of creating a graph for image segmentation. (a) Each small square represents a pixel in a colored image with i labelled and the surrounding patch colored according to RGB color layer. Radius r shows the maximum distance of pixel connectivity where only pixels within the ring have an edge weight connecting \mathcal{V}_i and \mathcal{V}_j , otherwise $\mathcal{W}_{ij} = 0$; (b) $m = 12$ random pixels are selected and transformed into graph (c) with $r = 2$, with edge weights from Eqs. (10-14).

For a colored image, we randomly sample m pixels. For each color layer, we consider each sampled pixel i and define a local patch encompassing it and its (up to) eight-way nearest neighbors, as depicted in Fig. 4(a). We define the sum of all N pixels in the patch as,

$$p_i = \sum_{n=1}^N i, \quad (8)$$

and the mean deviation between i and its neighbors as,

$$\ell_i = \sqrt{\frac{\sum_{n=1}^N (n - i)^2}{N}}, \quad (9)$$

where p_i and ℓ_i are calculated for all pixels in the image and are normalized over each color layer [53]. In addition to these local weights, we assign a global color weight, $c_i = M_A/M$, to each pixel according to its color frequency in the image, where A is the color of pixel i , M_A is the number of pixels with color A , and M is the total number of pixels. We define the edge weight connecting pixels i and j as \mathcal{W}_{ij} , which is equal to 0 if the pixel separation is greater than r . Otherwise, we define five methods for enumerating \mathcal{W}_{ij} based on a variety of techniques described in literature [53–58],

$$\text{Method 1: } \mathcal{W}_{ij} = \exp\left(\frac{|p_i - p_j|^q}{\sigma}\right); \quad (10)$$

$$\text{Method 2: } \mathcal{W}_{ij} = \exp\left(\frac{|c_i p_i - c_j p_j|^q}{\sigma}\right); \quad (11)$$

$$\text{Method 3: } \mathcal{W}_{ij} = \exp\left(\frac{|c_i - c_j|^q}{\sigma}\right); \quad (12)$$

$$\text{Method 4: } \mathcal{W}_{ij} = \exp\left(\frac{|i - j|^q}{\sigma}\right); \quad (13)$$

$$\text{Method 5: } \mathcal{W}_{ij} = \exp\left(\frac{|i c_i - j c_j|^q}{\sigma}\right). \quad (14)$$

Here, σ is the standard deviation in brightness across each patch, q is a free parameter and \mathcal{W}_{ij} is averaged over each color layer. To find the results of the image segmentation, we find the M3C of the graph $\mathcal{G} = (\mathcal{V}, \mathcal{W})$, with $|\mathcal{V}| = m$ vertices representing the sampled pixels with weights \mathcal{W}_{ij} connecting vertices i and j . We will show that the partition of the continuous phases in a polariton condensate graph (just like demonstrated in Fig. 2 for the house graph) into a ternary phase configuration, acting as decision variables for the M3C, can segment different objects within an image.

Using this approach, we show image segmentation for pictures of an apple and a tree over all five methods with $m = 200$, $r = 400$, $q = 0.1$ for the apple and $q = 0.2$ for the tree. r is selected to be at least the width of the object and q to scale the distribution of weights. We solve the M3C problem for each graph using the same procedure as described in Fig. 2 with the 0DGPE model for numerical efficiency in finding the XY ground state [see Eq. (A5) in the Appendix]. In Fig. 5 we show the partitioned spins overlaid on example images of an apple and a tree obtained from simulation. The XY ground state is obtained by simulating the polariton condensate network with weights (couplings) between different condensates determined by the image in question and the segmentation technique chosen from Eqs. (10)-(14). We can see that all methods successfully locate objects within each image. Methods 2 and 5, which include both local and global properties in their graph edge weights, best locate a single object and a background by predominantly cutting the graph into just two subsets, whereas Methods 1 and 4, which only consider local weights, segment the images into multiple objects. This is seen more clearly for the simpler apple image, where Methods 1 and 4 are able to locate the white background, black outline, red body and green leaf. Method 3 also segments the images into object and background by locating the dominant colors of the image, though some objects are located by multiple subsets, as only the global color distribution is considered in this method.

We also consider a simpler colored image with 25 pixels in Fig. 6 to demonstrate image segmentation using a planar graph. We first find the image segmentation again using the 0DGPE, with the all-to-all coupling between 25 pixels [see Fig. 6(a)], and a random sample of 5 pixels [see Fig. 6(b)], which correctly locates the different block

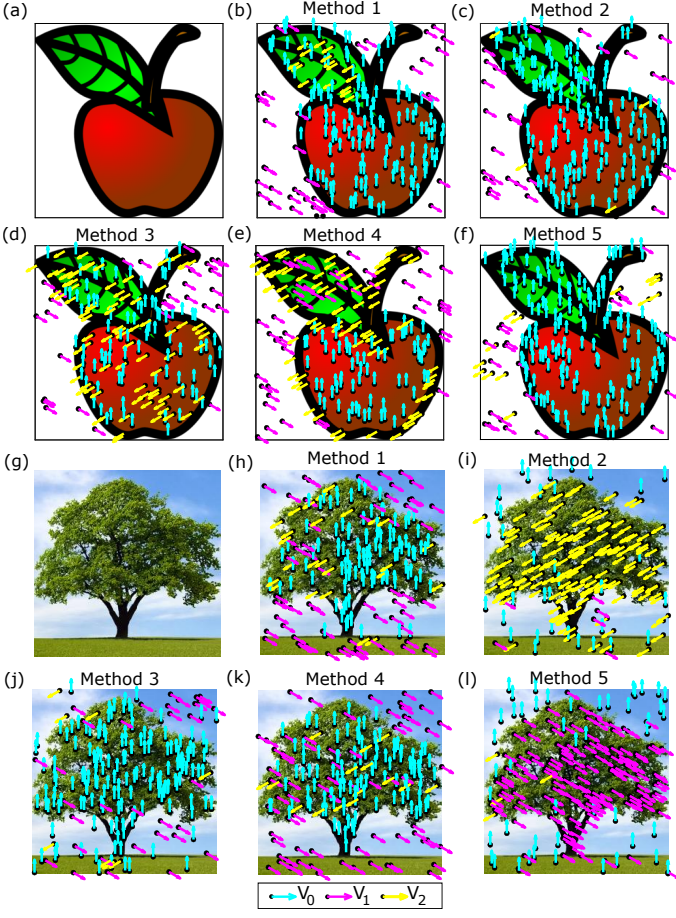


Figure 5. Images of (a) an apple and (g) a tree, with image segmentation results (b-f, h-l) using the 0DGPE for methods Eqs. (10)-(14) respectively, with $m = 200$, $r = 400$, $q = 0.1$ for (b-f) and $q = 0.2$ for (h-l). The cyan, magenta and yellow arrows represent the subsets $\mathcal{V}_{0,1,2}$ respectively.

colors in the image. As the sampled pixels are sparsely connected in the latter approach, the image segmentation can be represented by a planar graph, for which we find the M3C using the 2DGPE. The resulting 2D phase map in Fig. 6(c) shows the same segmentation calculated using the 0DGPE.

Constrained Via Minimization

Here we discuss the application of the M3C for constrained via minimization (CVM) in circuit design using polariton condensate networks. In order to optimise space, complex circuits are often split over multiple layers of a circuit board, where most applications require four to eight layers and smartphones tend to use around 12. Benefits of using multilayer circuit boards include higher assembly density, thinner boards, lighter weight and even better performance [59, 60]. The change in layer is achieved by drilling holes, known as “vias”, that are lined with a conductive coating, allowing the tracks to

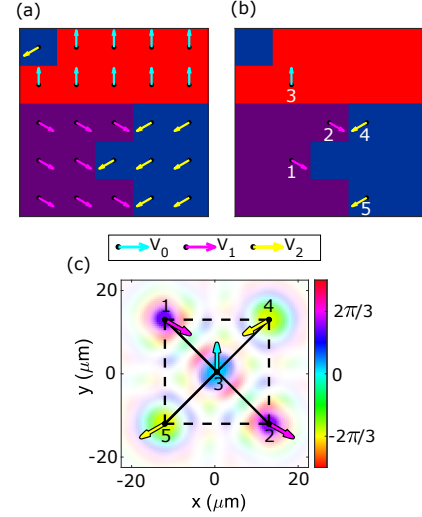


Figure 6. Simple colored image (a,b) showing image segmentation using the 0DGPE for the phase-discretized XY ground state of the graphs following Eq. (13), with $r = 4$, $q = 0.01$ for (a) $m = 25$ and (b) $m = 5$. (c) Shows the condensate phase map $\arg(\Psi(\mathbf{r}))$ obtained from 2DGPE simulation solving the set of pixels given by (b) with transparency proportional to the polariton density $|\Psi(\mathbf{r})|^2$. Projecting the phase of each condensate into its ternary counterpart is given by the cyan, magenta and yellow arrows, representing the subsets $\mathcal{V}_{0,1,2}$ respectively. Solid and dashed black lines represent $\mathcal{W}_{ij} = 1.0$ and $\mathcal{W}_{ij} = 0.8$ (rounded to 1 decimal place) respectively.

connect between multiple layers. Despite many benefits, the addition of vias increases production time, complexity, and cost, making it desirable to minimise the number of vias used in a multilayer circuit board.

For CVM, all cells are pre-placed and tracks are routed with the assumption that all pin connections are bipartite (i.e., a single track connects two pins), but layer assignment is not yet performed. Segments of track which overlap are labelled as critical segments which cannot be on the same layer of circuit board. Free segments of track have no overlap with other tracks and these are the regions in which vias can be placed. We demonstrate CVM through reducing the task to a M3C problem, following the methods and example in [38], which we then map to the phase-discretized XY model in order to solve with a network of polariton condensates.

For a circuit [see Fig. 7(a)], we define the layout graph $\mathcal{G} = (\mathcal{V}, \mathcal{E})$. Each critical edge is represented by a vertex in set \mathcal{V} , where pairs of vertices are connected by either a conflict edge \mathcal{A} (when a pair of critical segments cross paths) or by a continuation edge \mathcal{B} (when a pair of critical segments are connected by a free segment), such that $\mathcal{E} = \mathcal{A} \cup \mathcal{B}$. The layout graph of the example circuit is shown in Fig. 7(b). The conflict graph $\mathcal{C} = (\mathcal{V}, \mathcal{A})$ of \mathcal{G} can partition into connected bipartite components $(\mathcal{V}_i, \mathcal{A}_i)$ with i labelling the z critical regions of \mathcal{G} that are connected solely by critical edges. The reduced layout graph $\mathcal{R} = (\mathcal{S}, \mathcal{T})$ arbitrarily selects a vertex v_i in \mathcal{V}_i to

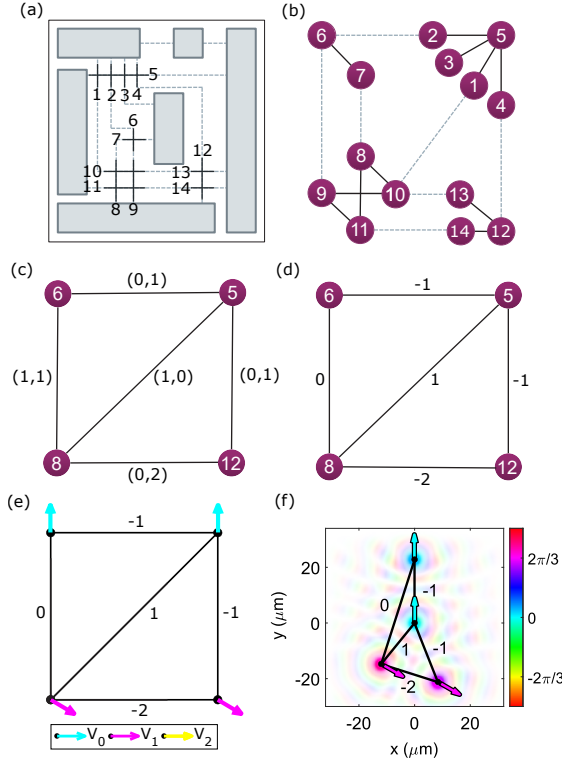


Figure 7. (a) A circuit with routing between pre-placed cells, with critical segments of tracks numbered and shown in solid black line and free segments showed in gray dashes; (b) the layout graph of circuit (a) with critical edges shown in solid black and continuation edges in gray dashes; (c) the reduced layout graph of (b) with edges labelled $(\alpha_{ij}, \beta_{ij})$; (d) the reduced layout graph of (b) with edge weights $w_{ij} = \alpha_{ij} - \beta_{ij}$, and (e,f) ground state discretized XY phase for the M3C of graph (d), solved using the 0D and 2DGPEs respectively, with black numbers representing the graph edge weights w_{ij} . The cyan, magenta and yellow arrows represent the subsets $\mathcal{V}_{0,1,2}$ respectively and in (f) the transparency is proportional to the polariton density $|\Psi(\mathbf{r})|^2$.

represent critical region i , such that $\mathcal{S} = \{v_i, \dots, v_z\}$. \mathcal{T} contains the edges linking v_i and v_j for $i \neq j$, if and only if \mathcal{G} contains a continuous edge connecting some vertex in \mathcal{V}_i to some vertex in \mathcal{V}_j . As continuation edges do not cross, \mathcal{R} is a planar graph. The edges of \mathcal{R} in Fig. 7(c) have weights $(\alpha_{ij}, \beta_{ij})$, as contained in \mathcal{T} , such that:

α_{ij} = Minimum number of vias needed between \mathcal{V}_i and \mathcal{V}_j should v_i and v_j be assigned the same layer, i.e. sum of all free segments between \mathcal{V}_i and \mathcal{V}_j that connect a pair of critical segments with different orientations (horizontal and vertical);

β_{ij} = Minimum number of vias needed between \mathcal{V}_i and \mathcal{V}_j should v_i and v_j be assigned different layers, i.e. sum of all free segments between \mathcal{V}_i and \mathcal{V}_j that connect a pair of critical segments with the same orientation.

The partition of this graph into \mathcal{S}_n , $n = 0, 1, 2$, corresponds to the assignment of each critical region to layer n . For such a partition, the number of vias required is

$$\text{VIA}(\mathcal{S}_n) = \sum_{v_i v_j \in \mathcal{T}_n} \alpha_{ij} + \sum_{v_i v_j \in \delta \mathcal{T}} \beta_{ij} \quad (15)$$

where edges \mathcal{T}_n connect critical regions assigned the same layer and $\delta \mathcal{T}$ connect critical regions assigned different layers. By defining $A = \sum_{v_i v_j \in \mathcal{T}} \alpha_{ij}$, then

$$\text{VIA}(\mathcal{S}_n) - A = \sum_{v_i v_j \in \delta \mathcal{T}} (\beta_{ij} - \alpha_{ij}). \quad (16)$$

As A is invariant on the layer assignment, and by redefining the edge weights $\mathcal{W}_{ij} = \alpha_{ij} - \beta_{ij}$ as in Fig. 7(d), we see that this problem follows the same form as Eq. (6). Thus, the constrained via minimization problem is reduced to the M3C problem of Eq. (7),

$$\max \sum_{v_i v_j \in \delta \mathcal{T}} \mathcal{W}_{ij}. \quad (17)$$

The phase-discretized XY solution coming from the polariton network for our example reduced layout graph [see Figs. 7(e,f)] partitions the vertices into just two subsets, showing that the minimum via configurations only requires two layers of circuit board. In this example, the minimized number of vias is 2, as $A - \sum_{v_i v_j \in \delta \mathcal{T}} \mathcal{W}_{ij} = 2 - 0$ and thus a correct solution has been found by the polariton network.

III. DISCUSSION

We have investigated possible future applications of driven-dissipative polariton condensate networks in solving optimization tasks by associating their phase degree of freedom with a ternary phase-discretized version of the XY model using a random hyperplane method [10]. The study is motivated by the condensate network's robust dynamical ability to stabilise into a stationary state with a phase configuration which near-optimally minimises the XY model [25, 31, 33], methods in semi-definite programming, and the general interest to design optical based solvers aimed at hard computational tasks. We study a direct mapping between the NP-Hard max-3-cut optimisation problem and the ternary phase-discretized XY model in the applications of image segmentation and CVM in circuit design which we solve using the driven-dissipative Gross-Pitaevskii equation describing the complex dynamics of microcavity polariton condensates. For image segmentation, we form a graph with vertices representing a sample of pixels and enumerate the edge weights using Eqs. (10)-(14). These different methods consider both local and global image features which can be selected and tuned based on the image features. For CVM, we follow the methods of [38] in reducing a circuit to

a graph which can be represented by a polariton network. Our work goes beyond previously studied Ising machines to solve the max-2-cut problem [19] by exploiting the continuous phase degree-of-freedom in oscillatory systems, whereby their natural tendency in minimizing the XY model can be applied to solve the M3C problem through Goemans and Williamson inspired semi-definite program. Our work applies to any dissipative oscillatory system such as laser networks and photonic condensates but in this study we have taken steps towards realizing a polaritonic system as practical optical computational devices by exploiting its fast optical timescales, parallel interactive nature, and continuous degree of freedom that can now be readily accessed in state-of-the-art experiments [61]. Currently the polariton system discussed here possesses limitations since only near neighbor condensates can interact through their mutual interference in the 2D microcavity system. This would make them more suited to obtain maximum cut solutions for planar graphs (sparsely connected vertices). However, maximum cut solutions can be obtained using a polynomially bounded algorithm for planar graphs and therefore the true strength of polariton systems relies on overcoming nearest neighbor coupling to help extend their applicability to non-planar graphs. With the recent advancements in both microcavity fabrication and experimental techniques, polariton condensates could be extended to multicavity systems with polaritons additionally coupling/interfering across different cavities making them much more suited for non-planar graph problems.

Appendix A: Polariton theory

The ground state of the XY model is obtained numerically through previously studied methods using the generalized GPE equation describing the dynamics of interacting polariton condensates [25]. The laser driven microcavity system is simulated close, but above, the condensation threshold where the interacting condensates (corresponding to their respective laser spots) are found to spontaneously self-organise into a phase configuration which maximises the particle number of the condensate which can be regarded as minimization of an effective XY model [26]. The polariton condensate wavefunction, $\Psi(\mathbf{r}, t)$, is described by the generalized GPE coupled to an active and inactive exciton reservoir [62]. The active reservoir, $n_A(\mathbf{r}, t)$, contains excitons which experience bosonic stimulated scattering into the condensates,

and is sustained by the inactive reservoir, $n_I(\mathbf{r}, t)$.

$$i\frac{\partial\Psi}{\partial t} = \left[-\frac{\hbar\nabla^2}{2m} + G(n_A + n_I) + \alpha|\Psi|^2 + \frac{i}{2}(Rn_A - \gamma) \right] \Psi, \quad (\text{A1})$$

$$\frac{\partial n_A}{\partial t} = -(\Gamma_A + R|\Psi|^2)n_A + Wn_I, \quad (\text{A2})$$

$$\frac{\partial n_I}{\partial t} = -(\Gamma_I + W)n_I + P(\mathbf{r}). \quad (\text{A3})$$

Here, m is the effective mass of a polariton in the lower dispersion branch, α is the interaction strength of two polaritons in the condensate, G is the polariton-reservoir interaction strength, R is the rate of stimulated scattering of polaritons into the condensate from the active reservoir, γ is the polariton decay rate, $\Gamma_{A,I}$ is the decay rate of active and inactive reservoir excitons respectively, W is the conversion rate between inactive and active reservoir excitons, and $P(\mathbf{r})$ is the non-resonant CW pump profile given by

$$P(\mathbf{r}) = P_0 \sum_i p(\mathbf{r} - \mathbf{r}_i). \quad (\text{A4})$$

Here, P_0 denotes the laser power density and the function $p(\mathbf{r})$ corresponds to the 2D annular shaped profile of a single laser incident onto the microcavity plane and the coordinates \mathbf{r}_i are the locations of the vertices in the polariton graph. The annular shaped pump profiles optically trap each condensate, yet allow for coherent transport of particles between nearest neighbors, consistent with those described in [33]. Graph weights are mapped to trap separation distances by scaling the graph weights to the maxima and minima of the imaginary component of the overlap integral between two optically trapped polariton condensates.

Equations (A1)-(A3) can be simplified by considering only weak nonlinear effects on the condensate saturation with its reservoir (dictated by parameter R) and that the characteristic reservoir timescales are much shorter than those of the condensate [63]. Under these assumptions and choosing an appropriate basis of condensate wavefunctions $\varphi_n(\mathbf{r})$, which are only weakly modified due to particle interactions, the total condensate wavefunction can be written as $\Psi(\mathbf{r}, t) = \sum_n \varphi_n(\mathbf{r})\psi_n(t)$. We then obtain a system of coupled 0DGPEs [26, 63] which model spatially independent polariton wavefunctions $\psi_n(t)$ that consists of a single point value for each condensate that varies over time coupled through J_{nm} ,

$$\frac{d\psi_n}{dt} = \left[P - \frac{\gamma}{2} - R|\psi_n|^2 \right] \psi_n + \sum_m J_{nm}\psi_m. \quad (\text{A5})$$

Here, P denotes the gain of each condensate centre coming from the nonresonant pumps and J_{nm} is the coupling strength determined by the interference and overlap between adjacent condensates [33]. We will assume that

blueshift coming from interactions α are negligible compared to the trap energy levels set by the pumping profile. Our simulations always start from random initial conditions and once the condensates ψ_n have converged to a steady state for a given $P > \gamma/2$ we extract their phases $\theta_n = \arg(\psi_n)$ to obtain the approximate ground state energy of Eq. (3). We perform numerical integration of Eqs. (A1)-(A3) and Eq. (A5) in time using a linear multistep method, for the 2D and 0DGPE respectively.

In the 2DGPE simulations, the parameters are taken such that the polariton mass and lifetime are based on the properties of a laboratory InGaAs microcavity sample: $m = 0.28 \text{ meV ps}^2 \mu\text{m}^{-2}$ and $\gamma = \frac{1}{5.5} \text{ ps}^{-1}$. We choose values of interaction strengths typical of InGaAs based systems: $\hbar\alpha = 7 \mu\text{eV } \mu\text{m}^2$, $G = 10\alpha$. The non-radiative recombination rate of inactive reservoir excitons

is taken to be much smaller than the condensate decay rate ($\Gamma_I = 0.01\gamma$), whereas the active reservoir is taken comparable to the condensate decay rate $\Gamma_A = \gamma$ due to fast thermalization to the exciton background [64]. The final two parameters are then found by fitting to experimental results where we use the values $\hbar R = 98.9 \mu\text{eV } \mu\text{m}^2$, and $W = 0.035 \text{ ps}^{-1}$. In the 0DGPE simulations, we use the parameters $\hbar R = 65.9 \mu\text{eV } \mu\text{m}^2$ and $\gamma = 0.1 \text{ ps}^{-1}$.

ACKNOWLEDGEMENTS

S.L.H., H.S. and P.G.L. acknowledge the support of the UK's Engineering and Physical Sciences Research Council (grant EP/M025330/1 on Hybrid Polaritonics).

-
- [1] C. Tardi, “Moore’s Law Explained,” (2019).
 - [2] B. Benchoff, “Gordon more: Exponential growth in linear time: The end of moore’s law,” (2015).
 - [3] S. DeCanio, *Economic Models of Climate Change: A Critique* (Springer, 2003).
 - [4] R. Ibsen-Jensen, K. Chatterjee, and M. A. Nowak, *Proceedings of the National Academy of Sciences* **112**, 15636 (2015).
 - [5] X. Zhang and I. Dincer, *Energy Solutions to Combat Global Warming* (Springer, 2016).
 - [6] P. B. Jayaraj, K. Rahamathulla, and G. Gopakumar, in *2016 IEEE International Parallel and Distributed Processing Symposium Workshops (IPDPSW)* (2016) pp. 580–588.
 - [7] N. A. Pierce and E. Winfree, *Protein Engineering, Design and Selection* **15**, 779 (2002).
 - [8] M. R. Garey and D. S. Johnson, *Computers and Intractability: A Guide to the Theory of NP-Completeness* (W. H. Freeman & Co., USA, 1990).
 - [9] D. G. Luenberger and Y. Ye, *Linear and Nonlinear Programming*, 4th ed., International Series in Operations Research & Management Science (Springer International Publishing, 2016).
 - [10] M. X. Goemans and D. P. Williamson, *J. ACM* **42**, 1115–1145 (1995).
 - [11] S. Zhang and Y. Huang, *SIAM Journal on Optimization* **16**, 871 (2006).
 - [12] F. P. Such, V. Madhavan, E. Conti, J. Lehman, K. O. Stanley, and J. Clune, *CoRR* **abs/1712.06567** (2017), [arXiv:1712.06567](https://arxiv.org/abs/1712.06567).
 - [13] X.-S. Yang, *Nature-Inspired Optimization Algorithms* (Elsevier, Amsterdam, Netherlands, 2014).
 - [14] C. A. Tovey, in *Recent Advances in Optimization and Modeling of Contemporary Problems*, INFORMS Tutorials in Operations Research (INFORMS, 2018) pp. 158–192.
 - [15] A. Aspuru-Guzik and P. Walther, *Nature Physics* **8**, 285 (2012).
 - [16] C. Sun, M. T. Wade, Y. Lee, J. S. Orcutt, L. Alloatti, M. S. Georgas, A. S. Waterman, J. M. Shainline, R. R. Avizienis, S. Lin, B. R. Moss, R. Kumar, F. Pavanello, A. H. Atabaki, H. M. Cook, A. J. Ou, J. C. Leu, Y.-H. Chen, K. Asanović, R. J. Ram, M. A. Popović, and V. M. Stojanović, *Nature* **528**, 534 (2015).
 - [17] A. Marandi, Z. Wang, K. Takata, R. L. Byer, and Y. Yamamoto, *Nature Photonics* **8**, 937 (2014).
 - [18] P. L. McMahon, A. Marandi, Y. Haribara, R. Hamerly, C. Langrock, S. Tamate, T. Inagaki, H. Takesue, S. Utsunomiya, K. Aihara, R. L. Byer, M. M. Fejer, H. Mabuchi, and Y. Yamamoto, *Science* **354**, 614 (2016).
 - [19] T. Inagaki, Y. Haribara, K. Igarashi, T. Sonobe, S. Tamate, T. Honjo, A. Marandi, P. L. McMahon, T. Umeki, K. Enbutsu, O. Tadanaga, H. Takenouchi, K. Aihara, K.-I. Kawarabayashi, K. Inoue, S. Utsunomiya, and H. Takesue, *Science* **354**, 603 (2016).
 - [20] T. Inagaki, K. Inaba, R. Hamerly, K. Inoue, Y. Yamamoto, and H. Takesue, *Nature Photonics* **10**, 415 (2016).
 - [21] O. Kyriienko, H. Sigurdsson, and T. C. H. Liew, *Phys. Rev. B* **99**, 195301 (2019).
 - [22] D. Pierangeli, G. Marcucci, and C. Conti, *Phys. Rev. Lett.* **122**, 213902 (2019).
 - [23] C. Roques-Carnes, Y. Shen, C. Zancoci, M. Prabhu, F. Atieh, L. Jing, T. Dubček, C. Mao, M. R. Johnson, V. Čeperić, J. D. Joannopoulos, D. Englund, and M. Soljačić, *Nature Communications* **11**, 249 (2020).
 - [24] M. Nixon, E. Ronen, A. A. Friesem, and N. Davidson, *Phys. Rev. Lett.* **110**, 184102 (2013).
 - [25] N. G. Berloff, M. Silva, K. Kalinin, A. Askitopoulos, J. D. Töpfer, P. Cilibizzi, W. Langbein, and P. G. Lagoudakis, *Nature Materials* **16**, 1120 (2017).
 - [26] P. G. Lagoudakis and N. G. Berloff, *New J. Phys.* **19**, 125008 (2017).
 - [27] Y. Takeda, Y. Takeda, S. Tamate, Y. Yamamoto, Y. Yamamoto, H. Takesue, T. Inagaki, S. Utsunomiya, and S. Utsunomiya, in *Frontiers in Optics 2017 (2017)*, paper **FM4E.3** (Optical Society of America, 2017) p. FM4E.3.
 - [28] I. Gershenzon, G. Arwas, S. Gadasi, C. Tradonsky, A. Friesem, O. Raz, and N. Davidson, *Nanophotonics*, 20200137 (2020).
 - [29] X.-Y. Xu, X.-L. Huang, Z.-M. Li, J. Gao, Z.-Q. Jiao, Y. Wang, R.-J. Ren, H. P. Zhang, and X.-M. Jin, *Science Advances* **6** (2020), [10.1126/sciadv.aay5853](https://doi.org/10.1126/sciadv.aay5853).

- [30] C. Tradonsky, I. Gershenzon, V. Pal, R. Chriki, A. A. Friesem, O. Raz, and N. Davidson, *Science Advances* **5** (2019), 10.1126/sciadv.aax4530.
- [31] K. P. Kalinin and N. G. Berloff, *Scientific Reports* **8**, 17791 (2018).
- [32] H. Goto, K. Tatsumura, and A. R. Dixon, *Science Advances* **5** (2019), 10.1126/sciadv.aav2372.
- [33] S. L. Harrison, H. Sigurdsson, and P. G. Lagoudakis, *Phys. Rev. B* **101**, 155402 (2020).
- [34] M. X. Goemans and D. P. Williamson, *Journal of Computer and System Sciences* **68**, 442 (2004).
- [35] M. R. Garey and D. S. Johnson, *Computers and Intractability: A Guide to the Theory of NP-Completeness* (W. H. Freeman & Co., USA, 1979).
- [36] F. Barahona, *J. Phys. A: Math. Gen.* **15**, 3241 (1982).
- [37] F. Harary, *Behavioral Science* **4**, 316 (1959).
- [38] F. Barahona, M. Grötschel, M. Jünger, and G. Reinelt, *Operations Research* **36**, 493 (1988).
- [39] F. Harary, M.-H. Lim, and D. C. Wunsch, *IMA J Management Math* **13**, 201 (2002).
- [40] C. Chiang, A. B. Kahng, S. Sinha, X. Xu, and A. Z. Zelikovsky, *IEEE Transactions on Computer-Aided Design of Integrated Circuits and Systems* **26**, 115 (2007).
- [41] S. de Sousa, Y. Haxhimusa, and W. G. Kropatsch, in *Graph-Based Representations in Pattern Recognition*, Lecture Notes in Computer Science, edited by W. G. Kropatsch, N. M. Artner, Y. Haxhimusa, and X. Jiang (Springer, Berlin, Heidelberg, 2013) pp. 244–253.
- [42] J. Rouco, E. Azevedo, and A. Campilho, *Sensors* **16**, 350 (2016).
- [43] F. Barahona, *SIAM J. Optim.* **6**, 823 (1996).
- [44] in *Graphs, Groups and Surfaces*, North-Holland Mathematics Studies, Vol. 8, edited by A. T. White (North-Holland, 1973) pp. 101 – 124.
- [45] E. de Klerk, D. Pasechnik, and J. Warners, *Journal of Combinatorial Optimization* **8**, 267 (2004).
- [46] S. K. S. S. K. Deb, B. Bhattacharyya, *Development of Intelligent Mathematical Modeling for Facilities Layout Design. Proceedings of the National Conference on Mathematical and Computational Models*. (Allied Publishers, 2001).
- [47] K. P. Kalinin and N. G. Berloff, *Phys. Rev. Lett.* **121**, 235302 (2018).
- [48] A. Frieze and M. Jerrum, *Algorithmica* **18**, 67 (1997).
- [49] D. J. Wales and J. P. K. Doye, *The Journal of Physical Chemistry A* **101**, 5111 (1997).
- [50] S. Petrov, “Image segmentation with maximum cuts,” (2005).
- [51] P. Sharma, “Image Segmentation | Types Of Image Segmentation,” (2019).
- [52] D. Martin, C. Fowlkes, D. Tal, and J. Malik, in *Proc. 8th Int’l Conf. Computer Vision*, Vol. 2 (2001) pp. 416–423.
- [53] X. Wang, C. Zhu, C.-E. Bichot, and S. Masnou, in *IEEE International Conference on Image Processing (ICIP)* (Melbourne, Australia, 2013) pp. 4064–4068.
- [54] P. F. Felzenszwalb and D. P. Huttenlocher, *International Journal of Computer Vision* **59**, 167 (2004).
- [55] B. Peng, L. Zhang, and D. Zhang, *Pattern Recognition* **46**, 1020 (2013).
- [56] Y. Boykov and G. Funka-Lea, *Int J Comput Vision* **70**, 109 (2006).
- [57] A. P. Eriksson, O. Barr, and K. Astrom, in *SSBA Symposium on Image Analysis* (2006).
- [58] I. M. Abdulqader and K. C. Lim, *Journal of Telecommunication, Electronic and Computer Engineering (JTEC)* **10**, 167 (2018).
- [59] “Multilayer PCB Benefits and Applications | PCBCart,” (2017).
- [60] “PCB Design Requirement for Smartphones | PCBCart,” (2018).
- [61] S. Alyatkin, J. D. Töpfer, A. Askitopoulos, H. Sigurdsson, and P. G. Lagoudakis, *Phys. Rev. Lett.* **124**, 207402 (2020).
- [62] M. Wouters and I. Carusotto, *Phys. Rev. Lett.* **99**, 140402 (2007).
- [63] N. Bobrovska and M. Matuszewski, *Phys. Rev. B* **92**, 035311 (2015).
- [64] M. Wouters, I. Carusotto, and C. Ciuti, *Phys. Rev. B* **77**, 115340 (2008).